Accelerated Ultraviolet Photoacoustic Microscopy Based on Optical Ultrasound Detection for Breast-Cancer Biopsy

Zehua Yu ⬤, Ziyu Ning ⬤, Changqiao Huang ⬤, Yizhi Liang ⬤, Long Jin ⬤, Yongjun Huang ⬤, Qingling Zhang ⬤, and Bai-Ou Guan ⬤

Abstract—Breast cancer often necessitates surgical interventions such as breast-conserving surgery or mastectomy. In these surgeries, sentinel lymph node (SLN) samples are often excised for histopathological examination to ascertain the presence of cancer metastasis. Despite its importance, traditional hematoxylin and eosin (H&E) staining, considerably prolongs the operation because of its complex processing requirements. Ultraviolet photoacoustic microscopy (UV-PAM) has emerged as a solution for bypassing the necessity of tissue staining or sectioning. However, its clinical application has been hindered by imaging speed. To overcome this challenge, we have developed a fast-scanning, reflection-mode UV-PAM designed for histopathology without staining based on high-sensitivity, wide-vision optical ultrasound detection. A specimen area of around 12 mm^2 can be scanned in 8 min with a lateral resolution of 1.5 μm. To enhance imaging speed, multi-focal PAM was implemented, resulting in a fourfold acceleration. This PAM technique has been utilized in SLN biopsy to differentiate cancerous tissue in breast cancer patients.

Index Terms—Photoacoustic microscopy, optical ultrasound sensor, label-free imaging.

Zehua Yu, Changqiao Huang, Yizhi Liang, Long Jin, and Bai-Ou Guan are with the Guangdong Provincial Key Laboratory of Optical Fiber Sensing and Communications, Institute of Photonics Technology, Jinan University, Guangzhou 510632, China, and also with the College of Physics & Optoelectronic Engineering, Jinan University, Guangzhou 510632, China (e-mail: liangyizhi88528@gmail.com).

Ziyu Ning is with the Guangdong Cardiovascular Institute, Guangdong Provincial People's Hospital (Guangdong Academy of Medical Sciences), Southern Medical University, Guangzhou 510080, China, also with the Department of Pathology, Guangdong Provincial People's Hospital (Guangdong Academy of Medical Sciences), Southern Medical University, Guangzhou 510080, China, and also with the Guangdong Provincial Key Laboratory of Artificial Intelligence in Medical Image Analysis and Application, Guangdong Provincial People's Hospital, Guangdong Academy of Medical Sciences, Guangzhou 510080, China.

Yongjun Huang is with the Department of Pathology, Guangdong Provincial People's Hospital (Guangdong Academy of Medical Sciences), Southern Medical University, Guangzhou 510080, China.

Qingling Zhang is with the Department of Pathology, Guangdong Provincial People's Hospital (Guangdong Academy of Medical Sciences), Southern Medical University, Guangzhou 510080, China, and also with the Guangdong Provincial Key Laboratory of Artificial Intelligence in Medical Image Analysis and Application, Guangdong Provincial People's Hospital, Guangdong Academy of Medical Sciences, Guangzhou 510080, China.

I. INTRODUCTION

BREAST cancer is the most prevalent cancer among women, accounting for 12% of all new cancer cases in 2020 [1]. The two primary surgical options for patients with breast cancer are mastectomy and breast-conserving surgery, with the goal of removing all cancerous tissue while preserving healthy tissue. Hematoxylin and eosin (H&E) staining provides histological information, aiding precise diagnoses and treatment choices. Sentinel lymph node (SLN) biopsy is frequently performed in breast cancer surgeries to ascertain the extent of the cancer and detect potential metastasis. The presence of cancer cells in SLNs may suggest the need for a more aggressive treatment plan, potentially encompassing additional surgery to remove the entire axillary lymph nodes (ALNs), followed by radiation therapy or chemotherapy. SLN biopsy can effectively avert unnecessary lymph node dissection, which can result in lymphedema and degrade the patient's quality of life [2]. However, current histopathological practices, which include tissue freezing, sectioning, and staining, can be laborious and time-consuming. Furthermore, these procedures may compromise the quality of histology slides because of tissue artifacts. Frozen section analysis may also exhibit varying levels of accuracy when compared to standard histological examinations, potentially resulting in subpar interpretation of tissue specimens.

Ultraviolet photoacoustic microscopy (UV-PAM) is an emerging imaging technology for diagnostics. It can produce histological images that mitigate the need for tissue staining or sectioning by visualizing DNA/RNA in the nucleus as intrinsic ultraviolet absorbers via ultrasound detection [3], [4], [5], [6], [7], [8], [9], [10], [11], [12], [13], [14], [15], [16].

Consequently, photoacoustic (PA) images, augmented with emerging machine learning methodologies, offer a high degree of similarity to microscopic images of H&E-stained tissue sections [6]. This similarity enables the differentiation between healthy and cancerous tissues in the brain, liver, bone, and breast. However, the application of UV-PAM is limited by the imaging time in the point-by-point raster-scanning method, which is
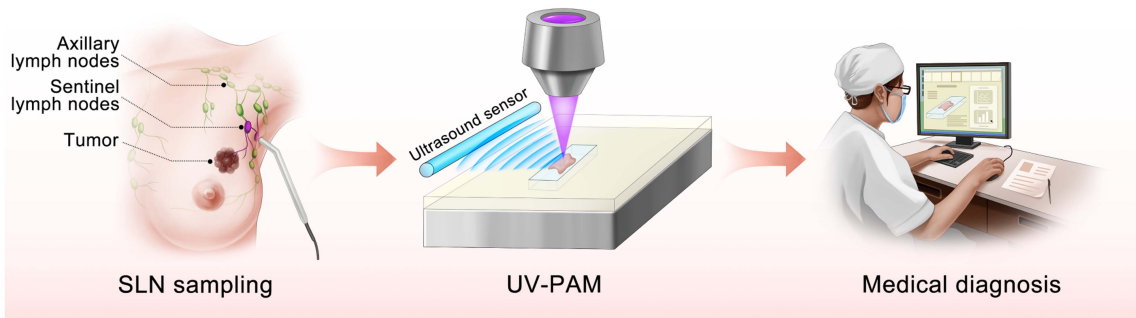
Fig. 1. Flowchart for SLN biopsy based on the UV-PAM enabled by optical ultrasound detection.

determined by the optical/ultrasound confocal configuration. For instance, imaging a 5 mm wide specimen section typically takes approximately 100 min [7]. While galvanometric scanning of the laser beam can effectively accelerate the imaging process, and the scanning range is strictly confined to approximately 50 μm within the acoustic focus [8]. An alternative solution involves using a waterproof 1-axis microelectromechanical systems (MEMS) scanner to simultaneously scan concurrently focused optical and acoustic beams [9]. To address the issue of imaging speed, multi-focal illumination was introduced using a micro-mirror array or a specialized diffractive grating. The optical absorptions at the individual foci were then retrieved and measured using a one- or two-dimensional array of ultrasonic transducers based on a back-projection acoustic reconstruction. By raster scanning the specimen, this illumination and detection process was repeated to cover the entire specimen, enabling a 1 cm $\times$ 1 cm area to be imaged in approximately 16 min [10]. This imaging scheme, which can be viewed as an integration of PAM and computed tomography, reduces the scanning time at the expense of complex optical illumination and ultrasound detection configurations, as well as a high-performance, costly data acquisition system. The ultraviolet photoacoustic remote sensing microscopy (UV-PARS) is to measure the PA signals by an all-optical approach [17], [13]. This optical-based UV-PARS can eliminate the needs of acoustic coupling and only need to scanning the optical beam. Although still limits by the laser repetition rate, combined with a self-developed fast UV pulse laser, it is one of the fastest UV-PAM system available. The additional optical probe beam in the UV-PARS system may increase the equipment cost and system complexity.

In this paper, we introduce a cost-effective strategy to enhance UV-PAM through optical ultrasound detection. The fiber-optic sensor offers a broad field of view, facilitating rapid laser beam scanning in a reflection-mode imaging system. This imaging configuration achieves a scanning speed of 1.46 mm²/min. Additionally, the wide detection field allows for the detection and differentiation of UV-induced ultrasound waves at various incident angles based on their distinct time-of-flights. This design enables the implementation of a multi-focal UV-PAM system that addresses optical absorption at multiple focal points simultaneously, resulting in a fourfold enhancement in imaging speed. We have applied this PAM technology to histopathological analysis of SLN biopsies in breast cancer patients, enabling

the identification of cancerous tissues within SLNs, indicative of cancer metastasis.

Fig. 1 presents a flowchart detailing the SLN biopsy process using accelerated UV-PAM. The SLNs, which are the initial lymph nodes to which cancer cells from the breast are likely to spread, can be identified by using a blue dye injected near the tumor or around the areola. Upon identification, the surgeon excises several SLNs through a small incision near the armpit for further examination. The obtained specimen is then prepared as 4-μm thick dewaxed sections for PA imaging. The PA images are then sent to pathologists for medical diagnosis and further treatment plans.

II. METHOD

A. Optical Ultrasound Detection

The ultrasound sensor incorporated in the UV-PAM is a distributed Bragg reflector fiber laser with a diameter of only 125 μm [18]. This laser cavity is created by incorporating two highly reflective Bragg gratings within an erbium-ytterbium codoped fiber, which provides optical feedback and gain to the laser. A 980-nm semiconductor laser, coupled with a 980/1550 nm wavelength multiplexer, is used to pump the laser. The signal light at 1550 nm, matching the Bragg wavelength of the gratings, is then amplified by a commercial erbium-doped fiber amplifier and directed to the photodetector.

Its lasing frequency varies in response to ultrasound waves, with acoustically induced shifts detected in the radiofrequency range. This detection is achieved by beating two orthogonal polarization modes of lasing, and the signal is captured by a high-speed photodetector before being digitized using a data acquisition card (JRF-2000, Jilishi Technologies, China). Subsequent phase variations are outputted through I/Q demodulation. Fig. 2(a) and b illustrate its frequency response and its noise-equivalent pressure density (NEPD) spectrum, showcasing its ultrasound detection capabilities. The sensor operates within an approximate bandwidth of 8 MHz, limited by the acoustic impedance mismatch due to the high rigidity of fiber glass. Its average NEPD across 30 MHz is approximately 1.5 mPa/Hz$^{1/2}$, and the sensor is among the most sensitive optical ultrasound sensors reported in literature. The noise-equivalent pressure (NEPD) and the working bandwidth provided by it are nearly two orders of magnitude lower than conventional electrical sensors
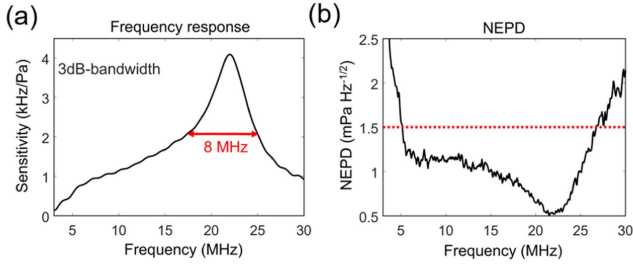
Fig. 2. (a) Frequency response of the laser sensor. (b) Measured noise-equivalent pressure density spectrum.
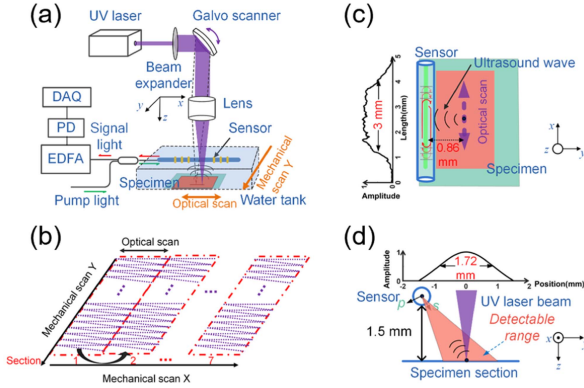

Fig. 3. (a) Schematic of the single-focal UV-PAM. (b) Scanning trajectory of single-focal system. (c) and (d) the coverage spans in the x- and y-directions offered by the laser sensor. EDFA, erbium-doped optical fiber amplifier; PD, photodetector; DAQ, data acquisition card.

of similar size [18], [19]. The highly sensitive fiber optic sensor is capable of operating in an afocal manner, providing a linear detection range and providing a fast scanning solution when paired with a galvanometric mirror.

B. Single-Focal UV-PAM System

Fig. 3 illustrates the schematic of the single-focal UV-PAM, highlighting the role of the optical ultrasound sensor in the imaging process. A 266-nm ultraviolet pulsed laser (WEDGE-HF 266, Bright Solutions, Italy) with a repetition rate of 48 kHz was used to illuminate the specimen. The laser beam was expanded and reflected by a galvanometric mirror (GVS411/M, Thorlabs) and focused on the specimen by using an objective lens (LMU-20X-UVB, Thorlabs Inc.). The diameter of the incident beam was approximately 4 mm, resulting an effective numerical aperture (N. A.) of $\sim$0.2. The UV-PAM utilized a line-shaped fiber-optic sensor for the detection of UV-induced PA signals. The laser beam was scanned by the galvanometric mirror, and the sensor was horizontally positioned in the x-direction, parallel to the laser beam scanning path. The specimen section, immersed in deionized water for acoustic wave coupling, underwent incremental motion along the y-axis using a motorized linear stage. Additionally, an extra linear stage in the x-axis direction was employed to ensure complete sample coverage during a hybrid scan [8]. Fig. 3(b) shows the scanning trajectory of single-focal system. The galvanometer mirror reflects the laser to perform

repetitive scans along the x axis at a round-trip rate of 30 Hz. The scanning range of an optical B-scan is $\sim$600 μm. The Y motorized stage is synchronized with the galvanometer mirror. When the galvanometer completes a B-scan, the Y motorized stage moves the sample along the y-direction with a step size of 0.75 μm. Following the completion of scanning for the preceding section of the specimen, the X motorized stage moves the sample along the x-axis with a step size of $\sim$562.5 μm, introducing an overlap of 37.5 μm for better alignment. The Y motorized stage and galvanometer mirror system are then synchronized for another scan. Single-focal system will stop, when the specimen is scanned completely.

Fig. 3(c) presents the extent of coverage in the x-direction of the UV-PAM system, determined by the intracavity optical intensity profile of the laser sensor. We have measured the maximum amplitude projection (MAP) from the B-scanned image of a black tape, which was used as a homogeneous UV absorber. The effective coverage span of the sensor is 3 mm which is determined by calculating the Full Width at Half Maximum (FWHM) of the signal. The sensitivity region is determined by the intracavity laser intensity profile [20]. Notably, due to the disparity between the sensor's line shape and the spherical wavefront of the UV-induced acoustic wave, only the portion normal to the fiber induces a lasing frequency shift. Consequently, when an acoustic source scans along the x-direction, the resulting optical response aligns with the local intracavity laser intensity. Nevertheless, the sensor is capable of providing sufficiently high sensitivity in the detection of the spherical ultrasound waves. Fig. 3(d) exhibits the coverage range in the y-direction, which is determined by the angular dependency of the laser sensor. The sensor possesses two orthogonal s- and p-polarized modes with a frequency difference of approximately 2 GHz. As a result, the acoustically induced frequency shift is detected in the radiofrequency range at the beat frequency. Moreover, the acoustic response follows a $\cos(2\theta)$ dependence with respect to the incident acoustic wave at θ. We assessed the sensor's sensitivity on the sample plane located at a distance of 1.5 mm and considered the FWHM as the indicative effective coverage range. Prior to scanning imaging, the sensor is rotated to align one of its principal axes (s- or p-polarization direction) with the acoustic incidence, as shown in Fig. 3(d). Importantly, this wide coverage enables the detection of ultrasound waves from various directions, which are generated at individual optical foci.

The laser scanning imaging was performed with a step size of 0.75 μm in both axes to satisfy the Nyquist sampling limit. We scanned 7 adjacent sections, each measuring 600 μm $\times$ 3 mm (800 pixels $\times$ 4000 pixels; x-axis $\times$ y-axis) with an overlap of around 37.5 μm (50 pixels) in x-axis. The 600 μm range was limited by the field of view of the image systems. By combining the 7 sections, the systems can cover field of view of 3.9 mm$\times$ 3 mm in 8 min.

The lateral resolution was assessed by imaging a 200 nm large gold nanoparticle (Fig. 4(a)) which defined by the full width at half maximum (FWHM) of the Gaussian fit, was measured at 1.5 μm. In addition, we fitted the envelope of the A-line PA signal, as shown in Fig. 4(b). The FWHM of the envelope is $\sim$109.4 ns, corresponding to an axial resolution of $\sim$164 μm.
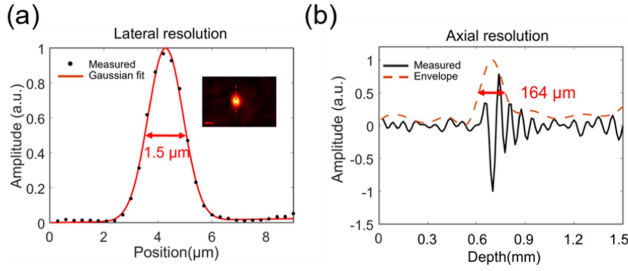
Fig. 4. (a) Lateral resolution with the inset that PA image of a 200 nm diameter gold nanoparticle. Black dots are the data along the red dotted line in the inset. (b) Axial resolution.
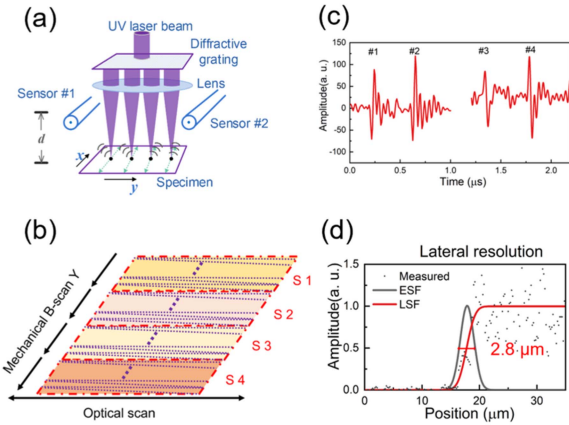

Fig. 5. Multi-focal UV-PAM. (a) Schematic. (b) Scanning trajectory of multi-focal system. (c) PA signals generated at the four laser foci. (d) Lateral resolution.

C. Multi-Focal UV-PAM System

To expedite the scanning speed, a multi-focal PAM was then implemented (Fig. 5(a)). We employed a bespoke one-dimensional diffractive grating (BSG1d4-266, Jiaqiang Opto-Electronics, China) that divided the UV laser beam into four beams with equal spacing and comparable intensities. The difference in the intensity of each beam is typically less than 20%. To address this discrepancy, our approach involves compensating the image signal based on the laser beam intensity difference. These beams were concurrently scanned along the x-axis using a galvanometric scanner, as the specimen was incrementally moved along the y-axis by the motorized stage. The objective lens was replaced with a long working distance lens (33954, Edmund Optics, focal length: 5 cm). The incident beam had a diameter of around 10 mm, resulting in an effective numerical aperture (N.A.) of 0.1. Fig. 5(b) presents the scanning trajectory of multi-focal system. We simultaneously scanned the four laser beams along the x-axis with a line scanning interval of ∼3 mm using galvanometric scanning at a round-trip rate of 6 Hz. The four laser beams are separated by 1mm in the y-direction. The Y motorized stage is synchronized with the galvanometer mirror and moves forward with a step size of 0.75 μm, when the galvanometer mirror finishes a B-scan. The scanning of the multi-focal system ended after the Y motorized stage moved by 1.0375mm (37.5 μm overlap).

As depicted in Fig. 5(c), within the y-z plane, the optical sensor can be viewed as a quasi-point acoustic detector, discerning UV-induced ultrasound waves based on their distinct time-of-flight. The temporal separation of the signals from the two foci is achieved due to the varying distances between each focus and the sensor, resulting in sequential arrival at the sensor and distinct temporal profiles in the time domain. This differentiation permits the precise identification and quantification of PA signals emanating from each UV laser beam. Furthermore, we utilized two photodetectors along with a dual-channel acquisition card. Each photodetector is dedicated to collecting signals from a specific sensor, ensuring accurate and simultaneous acquisition of data from the multiple focal points within the system. Notably, the sensor possesses an angular detection range of 60°. An additional sensor was used to expand the detection range and ensure full coverage of the imaging area.

We characterized the lateral resolution for the multi-focal UV-PAM. For the determination of lateral resolution, the edge of a sharp blade was imaged. The edge spread function (ESF) was acquired using MAP data from a B-scan. The ESF's first derivative produced a line spread function (LSF), whose full width at half maximum (FWHM) defined the lateral resolution, measured at 2.8 μm (Fig. 5(d)).

The parallel acquisition of multiple focus information is realized by time division multiplexing. The designated scanning regions S1 to S4 for each beam measured 3 mm× 1 mm (4000 × 1350 pixels; x-axis × y-axis), and this strategic approach reduced the imaging times to a mere 2 min, corresponding to a fourfold enhancement in imaging speed. Subsequently, we merged these quadrants to produce a complete PA image, with an overlap of 4000 × 50 pixels between the adjacent scanning regions. By combining the 4 parallel detection sections, the systems can cover field of view of 4 mm× 3 mm in 2 min.

D. Preparation of the Imaged Samples

The clinical SLN sections used in this work were retrospectively obtained from patients who had undergone SLN biopsies during breast cancer surgeries at Guangdong Provincial People's Hospital, with the institutional review board of GDPH providing a waiver for informed consent. To prepare the paraffin-embedded (FFPE) sections, SLN samples obtained during surgery were fixed in formalin for five hours. Subsequently, the samples underwent a series of procedures, including dehydration, clearing, and paraffin infiltration, before being embedded in paraffin wax. Slices with a thickness of 4 microns were obtained from the wax blocks, and two adjacent layers of the same tissue sample were selected for PA imaging and H&E staining, respectively. Prior to further experiments, the slides were baked in an oven at 70°C for 15 minutes.

For H&E staining, the samples were dewaxed using xylene, followed by sequential soaking in 100%, 95%, and 80% ethanol, as well as distilled water for 1 minute each. The slides were then immersed in a hematoxylin solution for 15 minutes, followed by a 2% lithium carbonate solution for 1 minute, and a 1% eosin solution for 40 seconds. After rinsing the slides with running water, they were dehydrated by soaking in 80%, 90%, 80%,
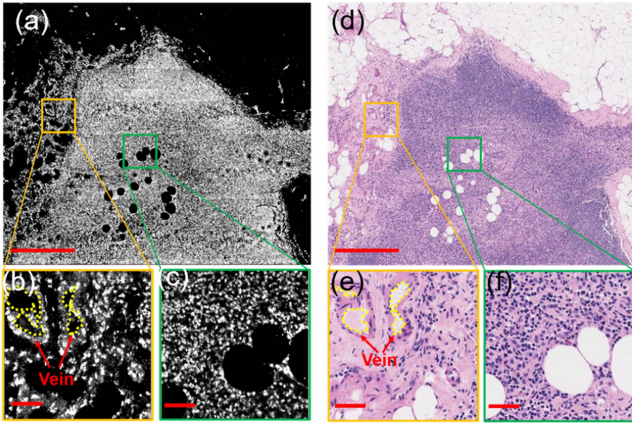
Fig. 6.   UV-PAM images (a)–(c) compared with H&E-stained histopathology (d)–(f) of clinical SLN specimens. Panels (b) and (e) are detailed views of the orange-box highlighted areas, with red arrows indicating veins. Panels (c) and (f) focus on the green-box highlighted regions. Scale bars are set at 500 μm for (a), (b) and 50 μm for (b), (c), (e), (f).

Fig. 8.   PA and H&E histopathology of clinical SLN specimens from breast cancer patient. (a) PA image. (b) H&E-stained image. (c) Magnified histoarchitectural features of the cancerous, normal, and boundary regions shown in the red, yellow, and green boxes in (a) and (b), respectively. The red dotted curves represent the boundaries between cancerous and normal areas. Scale bars: 500 μm (a), (b), 50 μm (c).
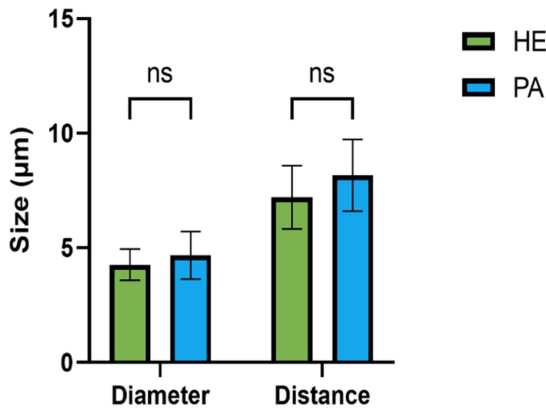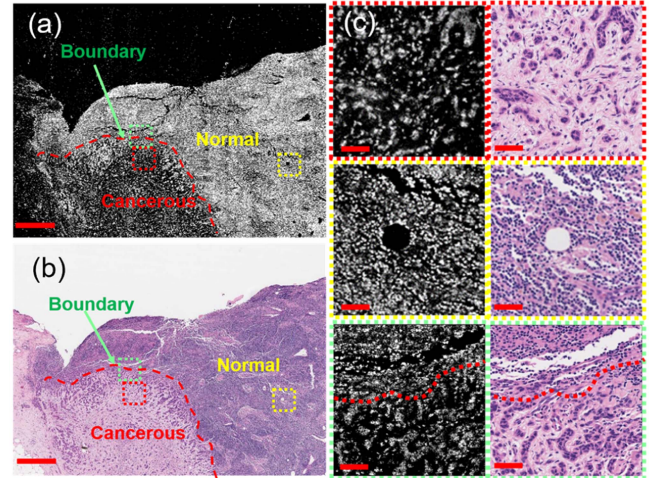

Fig. 7.   The statistics of nucleus-related morphology of health SLN sample, including nuclear diameter and nuclear spacing, showed that H&E-stained histopathology and UVPAM were highly consistent.

100% ethanol, and xylene for 1 minute each. H&E images were generated using a digital slide scanner (Leica GT450) equipped with a 40x objective lens (0.26 μm/pixel).

III. RESULT

A. Single-Focal UV-PAM System

Fig. 6 presents a PA image captured by the single-focal UV-PAM system alongside the corresponding H&E-stained histopathology of clinical SLN specimens. It allows for the identification of surrounding fibrous tissue and veins (refer to Fig. 6(b) and (e)). The images demonstrate consistent morphology and nuclei distribution (refer to Fig. 6(c) and (f)), with the lymphocyte cell nuclei (LCN) being uniformly distributed. The mean diameters of lymphocyte cell nucleus measured in the PA and H&E-stained images were 4.68 μm and 4.27 μm, respectively. And the mean nuclear spacing of lymphocyte cell nucleus measured in the PA and H&E-stained images were 7.21 μm and 8.17 μm, respectively (refer to Fig. 7). In our analysis process, the calculation methodology involves several

key steps. Initially, the image is transformed into a binary format by applying a threshold value set at 6 dB above the noise level. Subsequently, the nuclear center points post-binarization are identified using the erosion operation within a two-dimensional morphology algorithm. The diameter of each nucleus is then determined by measuring the distance from its center point to the edge of the binarized nuclear image. Additionally, to quantify nuclear spacing, we compute the distance between the center point of each nucleus and that of its neighboring nucleus. The statistics of nucleus-related morphology of health SLN sample, showed that H&E-stained histopathology and UV-PAM were highly consistent.

An image size of 3.9 mm× 3 mm (x-axis × y-axis) was captured within 8 minutes, resulting in an imaging speed of 1.46 mm^2/min (refer to Fig. 8). The UV-PAM leverages the nuclear absorption of ultraviolet light to reveal the nuclear distribution, thereby distinguishing between malignant and non-malignant regions. PA and H&E imaging results reflect similar morphology and distribution of nuclei. To detail these distinctions, we produced magnified maps of normal, transitional, and cancerous regions (Fig. 8(c)). The comparative analysis of PA and H&E-stained images showed a high degree of correlation between nuclear distribution and tissue architecture. Specifically, within the metastatic regions demarcated by the red dotted boxes, tumor cells showed organized patterns in cords, clusters, and trabecular formations, often with accompanying fibrosis. These neoplastic cells were markedly larger—approximately 1.5 to 2 times the size of nuclei in benign epithelial cells—and exhibited moderate nuclear atypia. Conversely, areas within the healthy lymph nodes, outlined by yellow dotted boxes, consisted of follicles and interfollicular spaces encircled by sinuses—characteristics indicative of a normal or benign lymph node. Furthermore, cells in these normal lymphatic regions were more homogeneously distributed than those in cancerous tissues. The increased cell
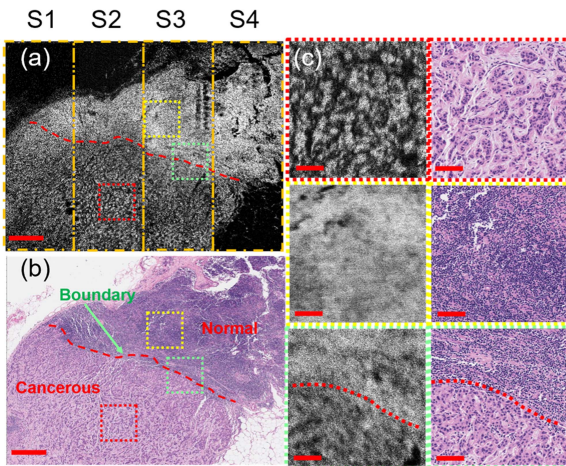
Fig. 9.   Multi-focal UV-PAM. (a)–(c) UV-PAM and H&E histopathology of clinical SLN specimens from breast cancer patient. (a) PA image. Regions S1 to S4 is parallelly image by different UV laser beam (b) H&E-stained image. (c) Magnified histoarchitectural features of the cancerous, normal, and boundary regions shown in the red, yellow, and green boxes in (a) and (b), respectively. The red dotted curves represent the boundaries between cancerous and normal areas. Scale bars: 500 μm (a), (b), 100 μm (c).
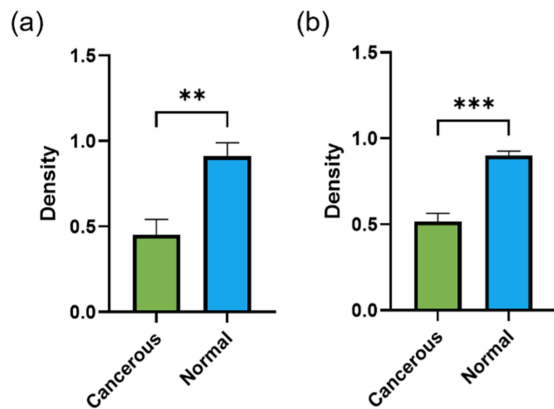

Fig. 10.   The statistics of density of health SLN sample, and cancerous SLN sample showed the differences between the nuclei of cancerous areas and healthy areas in (a) single-focal UVPAM and (b) multi-focal UV-PAM.

spacing observed in malignant areas led to a reduction in PA signal intensity, offering a potential biomarker for distinguishing between malignant and benign tissues.

B. Multi-Focal UV-PAM System

We employed the multi-focal PAM by imaging clinical SLN sections without staining to ascertain its efficacy and juxtapose these images with H&E-stained images of the contiguous tissue layers. The designated scanning regions S1 to S4 for each beam measured 3 mm$\times$ 1 mm (4000 $\times$ 1350 pixels;x-axis $\times$ y-axis). Subsequently, we merged these quadrants to produce a complete PA image, with an overlap of 4000 $\times$ 50 pixels between the adjacent scanning regions. Fig. 9 (presents a stitched PA image with dimensions of 3 mm $\times$ 4 mm (x-axis $\times$ y-axis). This strategic approach reduced the imaging times to a mere 2 min, corresponding to a fourfold enhancement in

imaging speed. Although its resolution has decreased, it is still able to observe the phenomenon of nuclear aggregation and heterosexual distribution in the cancerous area, so that it can be found to distinguish the carcinogenesis and even distinguish the dividing line between the carcinogenesis and the healthy area. We chose several different regions of the image and calculated the proportion of the nuclear signal area relative to the total area within each region. By averaging these values across the regions, we derived the nuclear density measurements for both the cancerous and normal regions, which can be seen in the statistical results in Fig. 10. Both single-beam and multi-beam imaging results show significant differences in the density nuclei between the cancer and normal region.

IV. CONCLUSION

In this Letter, we have showcased a reflection-mode UV-PAM system designed for Sentinel Lymph Node (SLN) biopsies in breast cancer surgeries. Our method combines highly sensitive fiber-optic ultrasound sensors with a wide field of view and superior detection sensitivity. This imaging approach significantly boosts scanning speed, allowing for imaging of an SLN section at a rate of 1.46 mm^2 per minute, limited only by the laser repetition rate. Additionally, we introduce multifocal PAM to address PA signals simultaneously generated at multiple focal points. The parallel acoustic detection effectively enhances imaging speed by fourfold, maintaining a resolution of 2.8 μm. Through UV-PAM, we achieved imaging quality comparable to H&E staining and successfully quantified nucleus size to effectively differentiate between cancerous and healthy tissues.

However, it is worth noting that the current lateral resolution of our multi-focus UV-PAM system is slightly lower compared to existing literature, primarily due to imperfections in the diffraction grating and aberrations induce by the long focal length objective lens. The current range of laser scanning is constrained by both the sensor's detectable area and the lens's field of view. With the use of current objective lens, our scanning range is limited to 600 μm for a single-focal scheme and 3 mm for a multi-focal scheme due to field curvature constraints. To mitigate these challenges, spatial filtering techniques for laser beams and high numerical aperture telecentric scanning lenses with flat image planes should be adopted to reduce these aberrations.

The limitation on the ultimate speed achievable in our multi-focal UV-PAM system is influenced by two key factors. Firstly, to utilize time division multiplexing effectively and separate signals from two foci, the distance between them must exceed 1 mm. With the field of view of the optical fiber sensor limited to approximately 2 mm (defined by a 60-degree receiving angle), a single sensor can only capture two laser foci simultaneously at maximum. The maximum range of laser foci is constrained by the field of view of the objective lens in the optical imaging system. Besides, due to field curvature effects, the current imaging setup can encompass around 4 mm, accommodating up to 4 foci. Augmenting the number of sensors and expanding the imaging system's field of view could enhance the system's capability to accommodate more laser foci.

While most UV-PAM reports are in transmission mode due to the large size of the piezoelectric transducer, making it inconvenient for imaging thick samples, our system operates in reflection mode. This versatility could potentially extend to imaging frozen sections and fresh tissues, offering significant advancements in histopathological practices. Notably, currently our demonstration was limited on wax-fixed sections which needs hours for sample preparation. We did not adopt frozen sections for research due to preservation issues. Our system's reflection mode operation opens up possibilities for UV-PAM to image both frozen and possibly fresh tissues [9], [16], [21]. Further enhancements involving modifications to the sample fixture to accommodate varying thicknesses and techniques like utilizing Bessel beams to enhance imaging quality and overcome the challenges posed by uneven samples are being considered. The compact size and adaptable positioning of the optical sensor make the present UV-PAM a highly promising solution for intraoperative diagnostics, facilitating informed surgical decision-making processes. Integrating such UV-PAMs into clinical settings could transform cancer treatment by offering immediate insights and critical guidance. Consequently, UV-PAM promises to become a vital tool, enhancing the abilities of medical professionals to improve patient outcomes and tailor therapeutic approaches more effectively.

ACKNOWLEDGEMENT

REFERENCES

[1] H. Sung et al., "Global cancer statistics 2020: GLOBOCAN estimates of incidence and mortality worldwide for 36 cancers in 185 countries," *CA: Cancer J. Clinicians*, vol. 71, no. 3, pp. 209–249, May 2021.

[2] A. E. Giuliano et al., "Effect of axillary dissection vs no axillary dissection on 10-year overall survival among women with invasive breast cancer and sentinel node metastasis: The ACOSOG Z0011 (alliance) randomized clinical trial," *Jama*, vol. 318, no. 10, pp. 918–926, Sep. 2017.

[3] J. Y. Kim, C. Lee, K. Park, S. Han, and C. Kim, "High-speed and high-SNR photoacoustic microscopy based on a galvanometer mirror in nonconducting liquid," *Sci. Rep.*, vol. 6, no. 1, Oct. 2016, Art. no. 34803.

[4] S. Jeon, J. Park, R. Managuli, and C. Kim, "A novel 2-D synthetic aperture focusing technique for acoustic-resolution photoacoustic microscopy," *IEEE Trans. Med. Imag.*, vol. 38, no. 1, pp. 250–260, Jan. 2018.

[5] T. T. Wong et al., "Label-free automated three-dimensional imaging of whole organs by microtomy-assisted photoacoustic microscopy," *Nature Commun.*, vol. 8, no. 1, Nov. 2017, Art. no. 1386.

[6] R. Cao et al., "Label-free intraoperative histology of bone tissue via deep-learning-assisted ultraviolet photoacoustic microscopy," *Nature Biomed. Eng.*, vol. 7, no. 2, pp. 124–134, Feb. 2022.

[7] T. T. Wong et al., "Fast label-free multilayered histology-like imaging of human breast cancer by photoacoustic microscopy," *Sci. Adv.*, vol. 3, no. 5, May 2017, Art. no. e1602168.

[8] X. Li, L. Kang, Y. Zhang, and T. T. Wong, "High-speed label-free ultraviolet photoacoustic microscopy for histology-like imaging of unprocessed biological tissues," *Opt. Lett.*, vol. 45, no. 19, pp. 5401–5404, Oct. 2020.

[9] J. W. Baik et al., "Intraoperative label-free photoacoustic histopathology of clinical specimens," *Laser Photon. Rev.*, vol. 15, no. 10, Oct. 2021, Art. no. 2100124.

[10] T. Imai, J. Shi, T. T. W. Wong, L. Li, L. Zhu, and L. V. Wang, "High-throughput ultraviolet photoacoustic microscopy with multifocal excitation," *Proc. SPIE*, vol. 23, no. 3, pp. 036007–036007, Mar. 2018.

[11] X. Li et al., "Ultraviolet photoacoustic microscopy with tissue clearing for high-contrast histological imaging," *Photoacoustics*, vol. 25, Mar. 2022, Art. no. 100313.

[12] W. Song et al., "Label-free identification of human glioma xenograft of mouse brain with quantitative ultraviolet photoacoustic histology imaging," *J. Biophotonics*, vol. 15, no. 5, May 2022, Art. no. e202100329.

[13] B. D. Cikaluk, B. S. Restall, N. J. M. Haven, M. T. Martell, E. A. McAlister, and R. J. Zemp, "Rapid ultraviolet photoacoustic remote sensing microscopy using voice-coil stage scanning," *Opt. Exp.*, vol. 31, no. 6, pp. 10136–10149, Mar. 2023.

[14] Y. Zhao, C. Guo, Y. Zhang, W. Song, C. Min, and X. Yuan, "Ultraviolet metalens for photoacoustic microscopy with an elongated depth of focus," *Opt. Lett.*, vol. 48, no. 13, pp. 3435–3438, Jul. 2023.

[15] W. Song et al., "Ultraviolet metasurface-assisted photoacoustic microscopy with great enhancement in DOF for fast histology imaging," *Photoacoustics*, vol. 32, Aug. 2023, Art. no. 100525.

[16] R. Cao et al., "Optical-resolution photoacoustic microscopy with a needle-shaped beam," *Nature Photon.*, vol. 17, no. 1, pp. 89–95, Jan. 2022.

[17] M. T. Martell et al., "Deep learning-enabled realistic virtual histology with ultraviolet photoacoustic remote sensing microscopy," *Nature Commun.*, vol. 14, no. 1, Sep. 2023, Art. no. 5967.

[18] Y. Liang et al., "Optical-resolution functional gastrointestinal photoacoustic endoscopy based on optical heterodyne detection of ultrasound," *Nature Commun.*, vol. 13, no. 1, Dec. 2022, Art. no. 7604.

[19] Y. Liang, J. Liu, L. Jin, B. O. Guan, and L. Wang, "Fast-scanning photoacoustic microscopy with a side-looking fiber optic ultrasound sensor," *Biomed. Opt. Exp.*, vol. 9, no. 11, pp. 5809–5816, Nov. 2018.

[20] F. Zhou, L. Jin, Y. Liang, L. Cheng, and B.-O. Guan, "Spatial sensitivity characterization of dual-polarization fiber grating laser sensors," *J. Lightw. Technol.*, vol. 33, no. 19, pp. 4151–4155, Oct. 2015.

[21] L. Kang, X. Li, Y. Zhang, and T. T. W. Wong, "Deep learning enables ultraviolet photoacoustic microscopy based histological imaging with near real-time virtual staining," *Photoacoustics*, vol. 25, Mar. 2022, Art. no. 100308.